Weidauer, Thomas; Schumacher, Jörg

Toward a mode reduction strategy in shallow moist convection

Original published in:
New journal of physics : the open-access journal for physics. - [Bad Honnef] : Dt. Physikalische Ges. - Bd. 15.2013 (Dez.), 125025, insges. 24 S.
Original published: 2013-19-12
ISSN (online): 1367-2630
DOI: 10.1088/1367-2630/15/12/125025
URL: http://dx.doi.org/10.1088/1367-2630/15/12/125025
[*Visited:* 2016-09-16]

New Journal of Physics
The open access journal for physics

Toward a mode reduction strategy in shallow moist convection

Thomas Weidauer[1,3] **and Jörg Schumacher**[2]

[1] Max-Planck-Institut für Meteorologie, Bundesstrasse 53, D-20146 Hamburg, Germany

[2] Institut für Thermo- und Fluiddynamik, Postfach 100565, Technische Universität Ilmenau, D-98684 Ilmenau, Germany

E-mail: thweidauer@gmail.com and joerg.schumacher@tu-ilmenau.de

New Journal of Physics **15** (2013) 125025 (24pp)
Received 6 June 2013
Published 19 December 2013
Online at http://www.njp.org/
doi:10.1088/1367-2630/15/12/125025

Abstract. The insufficient parameterization of low clouds which are caused by shallow convection remains one of the biggest sources of uncertainty in large-scale models of global atmospheric motion. One way to overcome this lack of understanding is to develop Boussinesq models of moist convection with simplified thermodynamics which allow for systematic studies of the cloud formation in different dynamical regimes and depend on a small set of system parameters only. This route makes the problem accessible to direct numerical simulations of turbulence without subgrid-scale modeling and provides an ideal testing bed for systematic and stepwise reductions of degrees of freedom. Such systematic reductions are studied here for a recently developed moist Rayleigh–Bénard convection model in the conditionally unstable regime. Our analysis is based on the proper orthogonal decomposition (POD) and determines the corresponding modes by a direct solution of the eigenvalue problem in form of an integral equation. The resulting reduced-order dynamical systems are obtained by a projection of the original equations of motion onto a finite set of POD modes. These modes are selected with respect to their energy as well as their ability to transport energy from large to small scales and to dissipate the

[3] New address: Dynardo GmbH, Steubenstrasse 25, D-99423 Weimar, Germany.

energy at smaller scales efficiently such that an additional modal viscosity can be omitted for most cases. The reduced models reproduce important statistical quantities such as cloud cover, liquid water flux and global buoyancy transport to a very good degree. Furthermore we investigate different pathways to reduce the number of degrees of freedom in the low-dimensional models. The number of degrees of freedom can be compressed by more than two orders of magnitude until the models break down and cause significant deviations of essential mean transport quantities from the original fully resolved simulation data.

Contents

1. Introduction

Moist turbulent convection and the resulting formation of clouds are not only omnipresent processes on Earth [1, 2] but also on our planetary neighbor Venus [3] and the giant gas planets, Jupiter [4] and Saturn [5]. Although many detailed aspects of cloud turbulence have been studied and reproduced in numerical simulations, a unifying theoretical framework of cloud formation and cloud dynamics parameterization is still missing. The latter is of central importance for more reliable predictions of the climate change in large-scale circulation models [6]. For example feedbacks of low marine clouds on the radiation balance or aerosol composition are still not well understood [7, 8]. Given the rapidly growing computational resources, one could therefore combine an increasing number of physical processes with a growing number of adjustable parameters and solve the resulting mathematical model equations on ever finer meshes. As reported from several such efforts (see e.g. Satoh *et al* [9]) cloud dynamics parameterizations developed for coarse grids can break down when moving to finer resolutions. The reason for this 'resolution gap' is that the coupling between resolved and unresolved turbulent dynamics is still not understood [10].

One can also follow an alternative route of abstracting the cloud formation dynamics from a number of particular processes and formulating a simplified mathematical model of moist Rayleigh–Bénard convection (MRBC) that contains the most important physical ingredients

and allows for systematic parameter studies which are accessible to direct numerical simulations (DNS) [11–14]. On the one hand, DNS studies of MRBC turn out to be still very demanding, in particular when larger Rayleigh numbers and extended layers with large aspect ratios are considered [14–16]. On the other hand, such models allow to formulate a generalized framework of moist convection in which fundamentally different stability regimes result, which can show similarities with simple wall-bounded shear flows [17, 18] and lead either to space-filling cloud layers or localized cloud aggregates [14]. The DNS model enables us also to reduce the complexity systematically and stepwise and to test how fluxes of heat and liquid water across the layer as well as the cloud formation and the cloud cover are affected by the decrease of the number of degrees of freedom or, in other words, the number of the modes. The latter aspect sets the central motivation for this work. To some degree, we are taking a pathway in an opposite direction compared to the discussion of the resolution gap. We will study the impact of insufficient resolution on global transport properties across the layer starting from well-resolved DNS.

In this work, we want to reduce the number of degrees of freedom in an MRBC model with a proper orthogonal decomposition (POD) technique, a method which has been used widely in free-shear and wall-bounded flows [19, 20] as well as thermal convection [21–23]. POD selects degrees of freedom with respect to their total energy and constructs a new orthonormal basis by solving an eigenvalue problem, which is formulated as an integral equation with a covariance matrix as the kernel. It is based on a record of high-resolution data obtained from simulations or experiments. This assures that we keep the most energetic convection patterns. Here, we want to solve this eigenvalue problem directly, extract the most energetic degrees of freedom and construct differently strongly reduced cloud formation models. Quantities such as the cloud cover or the buoyancy and liquid water fluxes are compared with the long-time evolution of the fully resolved DNS. These studies are conducted at different Rayleigh numbers such that we can provide the maximum data compression as a function of the Rayleigh number in an accessible range. Furthermore, we focus this analysis to convection at large aspect ratios (up to 32). This allows us also to study the impact of vertical mode reductions on the cloud and flow pattern formation. It should be mentioned here, that beside POD alternative methods are possible to detect dominating degrees of freedom from data sets and to construct reduced models on their basis, such as Laplacian eigenmaps with time-lagged embeddings [24] and stochastic clustering [25] or multi-scale models [26], to mention a few. It depends whether one is interested in a temporal or spatial evolution or both. The sensitivity with respect to spatial grid resolution has been also investigated in cloud resolving models, e.g. the resolution dependence of the parameterizations in [27] or of radiative–convective equilibrium states in [28].

The paper is organized as follows. In section 2 we discuss the moist convection model. The model equations in the Boussinesq approximation are formulated and the construction of the low-dimensional model (LDM) is outlined. In section 3, we discuss our results. In a first step, the vertical resolution is decreased followed by a sole horizontal reduction. In a third step, horizontal and vertical modes are jointly truncated. In all three cases, we investigate the impact of these reductions on global transport quantities. Afterwards, we explore dependencies of the mode reduction on Rayleigh number and aspect ratio. Finally, we will give an outlook and summarize our findings.

2. Cloud formation model

2.1. Moist Boussinesq equations

The moist convection model is a direct extension of classical Rayleigh–Bénard convection (see [29] for a recent review) incorporating the effect of phase changes between liquid water and vapor. This means that the present model also uses the Boussinesq approximation in which the height of the convection layer H is much smaller than the scale height of the atmosphere. The moist air can then be approximated as an incompressible fluid. Furthermore, we exclude the formation of rain which means that the total water content q_T, the sum of vapor and liquid water contents, q_v and q_l, is conserved. The complex thermodynamics of phase changes manifests in a nonlinear equation of state that describes the buoyancy B as a function of (potential) temperature (or entropy), total water content and height, $B(T, q_\mathrm{T}, z)$. It is simplified to a piecewise linear equation of state on both sides of the phase boundary. This simplification preserves the discontinuity of partial derivatives of the buoyancy of air parcels with respect to state variables and thus the latent heat release [12]. One can now reformulate the linearized equation of state $B(T, q_\mathrm{T}, z)$ in terms of two buoyancies and height, $B(D, M, z)$ which are denoted as the *dry* and *moist* buoyancy, D and M, respectively. Unsaturated or saturated air will contribute differently to the fluid motion in the layer of height H. Both fields determine the buoyancy B in an explicit saturation condition which has to be evaluated for each time step at each grid point. It is given by

$$B(\mathbf{x}, t) = \max[M(\mathbf{x}, t), D(\mathbf{x}, t) - N_\mathrm{s}^2 z], \tag{1}$$

where N_s is a Brunt–Vaisala frequency composed of the dry and moist adiabatic lapse rates. In a nutshell, the two buoyancy fields characterize the two components of the atmosphere, liquid water and unsaturated vapor. Their prescribed values at the top and bottom control if saturated or subsaturated conditions are sustained. It was shown that the model can be operated in different stability regimes [14]. In the linearly unstable regime, D and M are on average unstably stratified. This regime is similar to the dry convection case and results in space-filling turbulence. If dry air parcels are stably stratified while moist air parcels are unstably stratified, conditionally unstable convection is established which is relevant for the formation of cumulus clouds in the atmosphere [30]. The equations of motion are given by

$$\frac{\partial \mathbf{u}}{\partial t} + (\mathbf{u}\cdot\nabla)\mathbf{u} = -\nabla p + \sqrt{\frac{Pr}{Ra_\mathrm{M}}}\nabla^2\mathbf{u} + B\mathbf{e}_z, \tag{2}$$

$$\nabla\cdot\mathbf{u} = \mathbf{0}, \tag{3}$$

$$\frac{\partial D'}{\partial t} + (\mathbf{u}\cdot\nabla)D' = \frac{1}{\sqrt{Pr\,Ra_\mathrm{M}}}\nabla^2 D' + \frac{Ra_\mathrm{D}}{Ra_\mathrm{M}}u_z, \tag{4}$$

$$\frac{\partial M'}{\partial t} + (\mathbf{u}\cdot\nabla)M' = \frac{1}{\sqrt{Pr\,Ra_\mathrm{M}}}\nabla^2 M' + u_z\,. \tag{5}$$

The two scalar transport equations are given in terms of the deviations from the diffusive equilibrium, D' and M' respectively. Three dimensionless parameters arise in equations (2)–(5). The Prandtl number is defined as

$$Pr = \frac{\nu}{\kappa}, \tag{6}$$

and fixed to a value of 0.7. The dry and moist Rayleigh numbers are defined as

$$Ra_{\mathrm{M}} = \frac{(M_0 - M_H)H^3}{\nu\kappa}, \quad Ra_{\mathrm{D}} = \frac{(D_0 - D_H)H^3}{\nu\kappa}, \tag{7}$$

where D_0, D_H, M_0 and M_H are the prescribed buoyancy values at $z = 0$ and H. Quantities ν and κ denote the kinematic viscosity and the thermal diffusivity, respectively. The two advection–diffusion equations for M' and D' are not independent. This was shown first by Bretherton [11] and holds when physical processes such as rainfall and radiative cooling are not incorporated. Then the two buoyancy fields can be recombined to one advection–diffusion equation for a conserved scalar. In the following, we can therefore take

$$D'(\mathbf{x}, t) = \frac{Ra_{\mathrm{D}}}{Ra_{\mathrm{M}}} M'(\mathbf{x}, t). \tag{8}$$

The dry buoyancy field is thus determined by the moist buoyancy field[4]. In other words, the fluctuations of both fields are synchronized. Two more dimensionless parameters are hidden in the saturation condition (1), the amount of cloud water at $z = 0$ and H denoted CW_0 and CW_H, respectively,

$$CW_0 = \frac{M_0 - D_0}{N_{\mathrm{s}}^2 H}, \quad CW_H = 1 + \frac{M_H - D_H}{N_{\mathrm{s}}^2 H}. \tag{9}$$

Water deficit at the boundaries corresponds with negative values of CW_0 and CW_H while a sustained water content with positive ones. Throughout this work we will choose a static equilibrium such that the whole equilibrium layer is neither saturated nor subsaturated, i.e. $\overline{M}(z) = \overline{D}(z) - N_{\mathrm{s}}^2 z$ (see figure 1(a)). As a further consequence of (1), liquid water content is present in the turbulent layer when

$$q_{\mathrm{l}}(\mathbf{x}, t) = M(\mathbf{x}, t) - (D(\mathbf{x}, t) - N_{\mathrm{s}}^2 z) > 0. \tag{10}$$

The moist Boussinesq equations are solved in the volume $\Omega = L_x \times L_y \times H = \Gamma H \times \Gamma H \times H$ by a standard pseudo-spectral scheme with Fourier–Chebyshev expansions [16]. Similar to [11, 31] we apply free-slip boundary conditions for the velocity at the top and bottom planes. Laterally, periodic boundary conditions are applied for all fields. Γ denotes the aspect ratio of the layer and is set to values of 8, 16 and 32. The conditionally unstable equilibrium is perturbed by a finite-amplitude field and relaxes after a longer transient into a statistically stationary turbulent state. It is this flow state which will be used for the LDM derivation.

Our configuration can be thought as a very simplified setting for an atmospheric layer with an isothermal ocean surface as the lower lid and an upper lid which can be considered as a strong temperature inversion (see sketch in figure 1(b)). In particular, the upper rigid lid is a significant simplification. Note that even for a strong inversion layer vertical motion above the inversion would be possible. Standard mesoscale large-eddy simulation codes apply here a free-outflow boundary condition on a grid that is increasingly stretched toward the boundary and enhances numerical diffusion (see e.g. [32]). The advantage of our model is that the boundary conditions

[4] The dry buoyancy D corresponds with the liquid water potential temperature θ_{l} which equals the potential temperature θ when the air parcels are unsaturated. The moist buoyancy M corresponds with the equivalent potential temperature θ_{e}. The frequently used Paluch diagram representation $(q_{\mathrm{T}}, \theta_{\mathrm{e}})$ translates consequently into an (D, M) diagram via $\theta_{\mathrm{l}} = \theta_{\mathrm{e}} - L_v q_{\mathrm{T}}$ with the latent heat L_v.

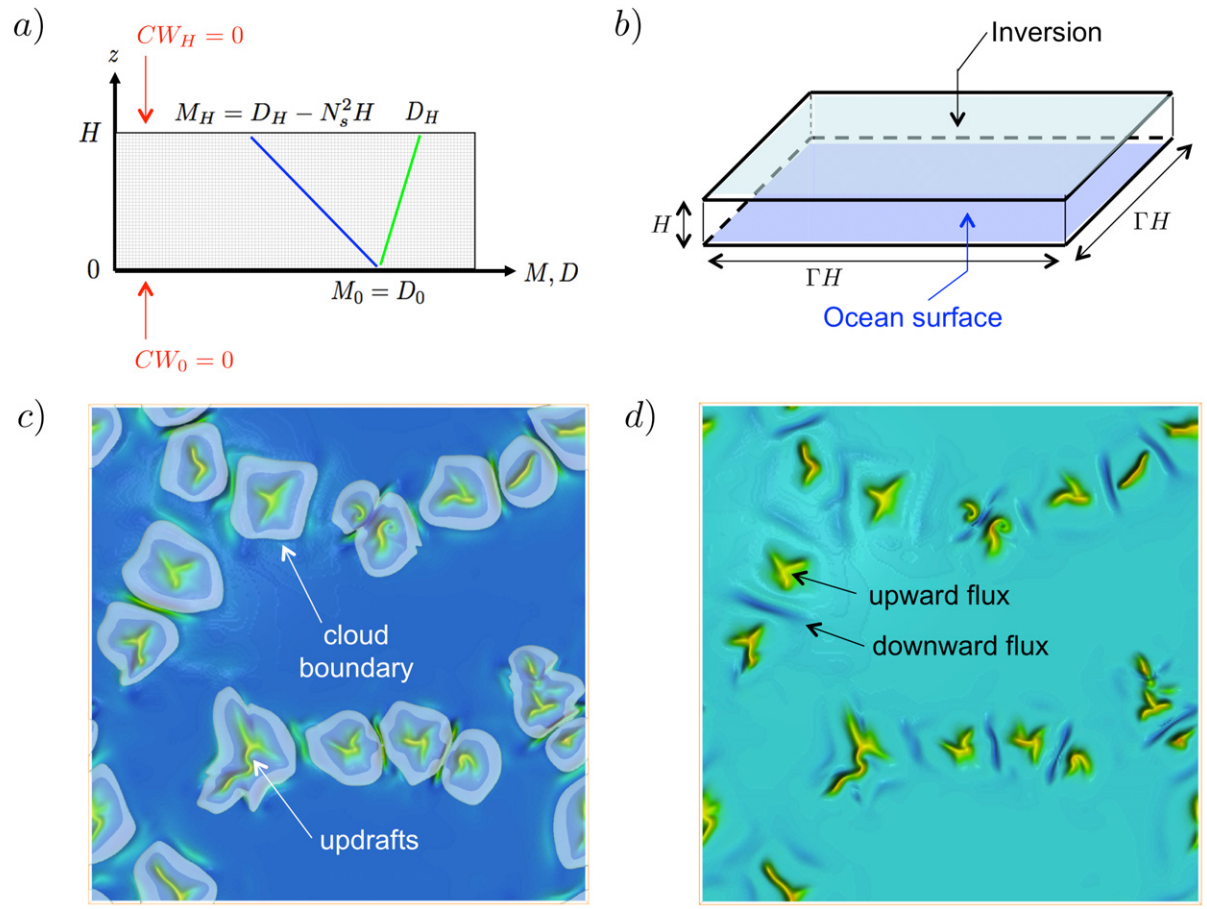

Figure 1. Moist convection layer. (a) Sketch of the conditionally unstable equilibrium state without fluid motion that serves as the initial condition. It is characterized by the linear profiles $\overline{D}(z) = D_0 + (D_H - D_0)z/H$ and $\overline{M}(z) = M_0 + (M_H - M_0)z/H$, respectively. The amplitudes of the dry and moist buoyancies are chosen such that $CW_0 = CW_H = 0$. The whole slab is thus neither saturated nor subsaturated (similar to [11]). (b) Sketch of the simulation domain. The bottom plane can be thought as an ocean surface while the top plane could correspond to a first approximation to a strong temperature inversion. The volume is $\Omega = \Gamma H \times \Gamma H \times H$. (c) Snapshot of the DNS at $\Gamma = 32$ (run DNS3 from table 1). A view from the top onto the whole layer is displayed. The cloud boundaries are shown as transparent isosurfaces together with the product $u_z q_l$ in the plane $(x, y, z = H/2)$. The latter is a measure for the local liquid water flux. (d) Same data as (c). The corresponding local convective buoyancy flux $u_z B$ is now displayed (again view from top and same data as in (c)).

are well-defined and allow thus for an application of the mode reduction techniques which will be presented in the following.

Typical heights under atmospheric conditions for such a shallow moist convection layer are $H \approx 2\,\mathrm{km}$. Since we conduct DNS without subgrid small-scale parameterizations of the turbulent fields, the accessible Rayleigh numbers are by more than ten orders of magnitude

lower than those in the real atmosphere. In [34], we have calculated how our system translates into a real shallow moist convection layer and estimated which turbulent diffusivity and viscosity would follow when such a layer is resolved by present grids.

2.2. Low-dimensional model construction

The turbulent fields of the moist convection problem are summarized into a four-component vector field $\mathbf{v} = (u_x, u_y, u_z, M')^{\mathrm{T}} \in L_2(\Omega)$. The idea of the POD method is to identify the smallest orthonormal subspace (or submanifold) of the underlying function space $L_2(\Omega)$ that represents all essential flow structures. This subspace has significantly less degrees of freedom compared to the full phase space that captures the flow fields in the DNS. The reduction of degrees of freedom in a LDM is done in three steps [20]:

- Construction of the set of orthonormal POD modes from a sequence of fully resolved DNS snapshots.
- Projection of the Boussinesq equations of moist convection onto the eigenspaces spanned by the individual POD modes.
- Truncation to a LDM spanned by the most energetic POD modes.

2.2.1. POD mode construction. The space $L_2(\Omega)$ is associated with the following inner product, denoted as $(\cdot, \cdot)_{L_2}$, and norm (the asterisk indicates complex conjugate):

$$E = \frac{1}{2}(\mathbf{v}, \mathbf{v})_{L_2} = \frac{1}{2}\int \mathbf{v}\,\mathbf{v}^* \mathrm{d}^3\mathbf{x} = \frac{1}{2}\,\|\mathbf{v}\|^2, \tag{11}$$

which is associated with a total energy. The energy E combines kinetic energy and scalar variance of the four fields which are dynamically coupled in our moist convection model. It follows as the canonical norm for the four-vector fields $\mathbf{v}$ in the Hilbert space $L_2(\Omega)$. Since the fields u_x, u_y, u_z and M' are dynamically coupled they also have to be analyzed jointly in the POD framework (see [22] or further references in [23] for dry convection). Other choices are possible, e.g. with inner products that give different weights to velocity and scalars. The task is now to extract a set of orthogonal functions $\{\phi^i\}_{i=1,\ldots}$ from the data which maximizes on average the following functional:

$$\frac{\langle|(\mathbf{v}, \phi^i)_{L_2}|^2\rangle_t}{\|\phi^i\|^2} \rightarrow \max. \tag{12}$$

The brackets $\langle\cdot\rangle$ denote an average, subscripts t, V and A stand for time average, volume average and horizontal plane average, respectively. The problem can be reformulated into an eigenvalue problem in form of an Euler–Lagrange integral equation [19] which is given in a general notation as follows:

$$\int_\Omega \langle \mathbf{v}(\mathbf{x}, t) \otimes \mathbf{v}(\mathbf{x}', t)\rangle_t\, \phi(\mathbf{x}')\, \mathrm{d}^3\mathbf{x}' = \lambda\phi(\mathbf{x}). \tag{13}$$

This Fredholm equation of second kind is discretized in space and time and then solved directly in our case. The eigenvalues are total energies of the corresponding eigenvectors; in our case a combination of kinetic energy and moist buoyancy variance. For the calculation of the kernel $\langle \mathbf{v}(\mathbf{x}, t) \otimes \mathbf{v}(\mathbf{x}', t)\rangle_t$ up to 600 statistically independent DNS snapshots were used in our specific application. Discrete symmetries, the rotation about $x = y = 0$ and reflection at the plane $x = 0$,

are used to increase the number of snapshots by a factor of 8 without performing additional DNS runs. The translational symmetry in the horizontal directions due to the periodic boundary conditions results in a mode structure for which the classical Fourier modes are the canonical choice in the horizontal directions. This POD mode ansatz is used in many other applications, such as in plane shear flows [33] or dry convection [23]. In our system, the general notation for the POD mode, ϕ, specifies then to the following. The modes are characterized by the wave vectors $\boldsymbol{k} = (k_x, k_y)$ and by a quantum number $\hat{k}$ with respect to the vertical direction. Each mode is uniquely determined by this triple and the ordering of the mode set is done with respect to their energy. In detail, they are given by

$$\boldsymbol{\Phi}_{\boldsymbol{k}}^{(\hat{k})}(\mathbf{x}) = \frac{\phi_{\boldsymbol{k}}^{(\hat{k})}(z)}{\sqrt{L_x L_y}} \exp\left(\frac{2\pi \mathrm{i} k_x x}{L_x} + \frac{2\pi \mathrm{i} k_y y}{L_y}\right). \tag{14}$$

Once the eigenfunctions are calculated, the original turbulence vector field $\mathbf{v}$ can be expressed in terms of these orthonormal functions

$$\mathbf{v}(\mathbf{x}, t) = \sum_{\boldsymbol{k}, \hat{k}} a_{\boldsymbol{k}}^{(\hat{k})}(t) \boldsymbol{\Phi}_{\boldsymbol{k}}^{(\hat{k})}(\mathbf{x}). \tag{15}$$

Note, that the expansion coefficients $a_{\boldsymbol{k}}^{(\hat{k})}(t)$ are the same for the velocity vector field $\mathbf{u}$ and the moist buoyancy field M'. The POD modes inherit linear properties of the original data, such as boundary conditions and incompressibility. In figure 2, we show how the incremental dilution of the number of POD modes, which are taken to reconstruct the original data, affects the liquid water content (upper row) and the vertical velocity fluctuations (lower row) starting from the DNS snapshot in panels (a) and (e). Even when the number of degrees of freedom (or modes), which is denoted as N_{DoF}, is decreased by more than two orders of magnitude, the liquid water content patterns are reproduced quite well. This is not the case for the vertical velocity component. Since the contour plot color coding in all figures is the same, one can see that up- and downdrafts decrease in amplitude.

2.2.2. Projection onto Boussinesq equations and Galerkin truncation. The derivation of the LDM from POD modes is straightforward. The original Boussinesq equations (2) to (5) are projected subsequently onto the orthogonal eigenspaces which are spanned by the individual POD modes using the scalar product (11). The original system of partial differential equations is transformed into a nonlinear coupled system of ordinary differential equations for the expansion coefficients which can be formally written as

$$\frac{\mathrm{d}a_{\boldsymbol{k}}^{(\hat{k})}}{\mathrm{d}t} = \sum_{\substack{\boldsymbol{p}=\boldsymbol{k}-\boldsymbol{q} \\ \hat{p}=\hat{k}-\hat{q}}} N(\boldsymbol{k}, \boldsymbol{q}, \hat{k}, \hat{q}) a_{\boldsymbol{q}}^{(\hat{q})} a_{\boldsymbol{p}}^{(\hat{p})} + L(\boldsymbol{k}, \hat{k}) a_{\boldsymbol{k}}^{(\hat{k})} + B(\boldsymbol{k}, \hat{k}). \tag{16}$$

The first term on the right hand side summarizes the quadratic nonlinearties arising from the advective terms in the original Boussinesq equations. The second term contains the linear contribution which results from the dissipation and the final term is due to the buoyancy. Note that the buoyancy in equation (1) can only be evaluated in physical space. Therefore, coefficients $B(\boldsymbol{k}, \hat{k})$ depend also on all expansion coefficients. This requires transformations between expansion space and physical space for the buoyancy contribution $B(\boldsymbol{k}, \hat{k})$ in (16) which contribute significantly to the required integration time. For time integration a fifth-order Adams–Bashforth scheme in used.

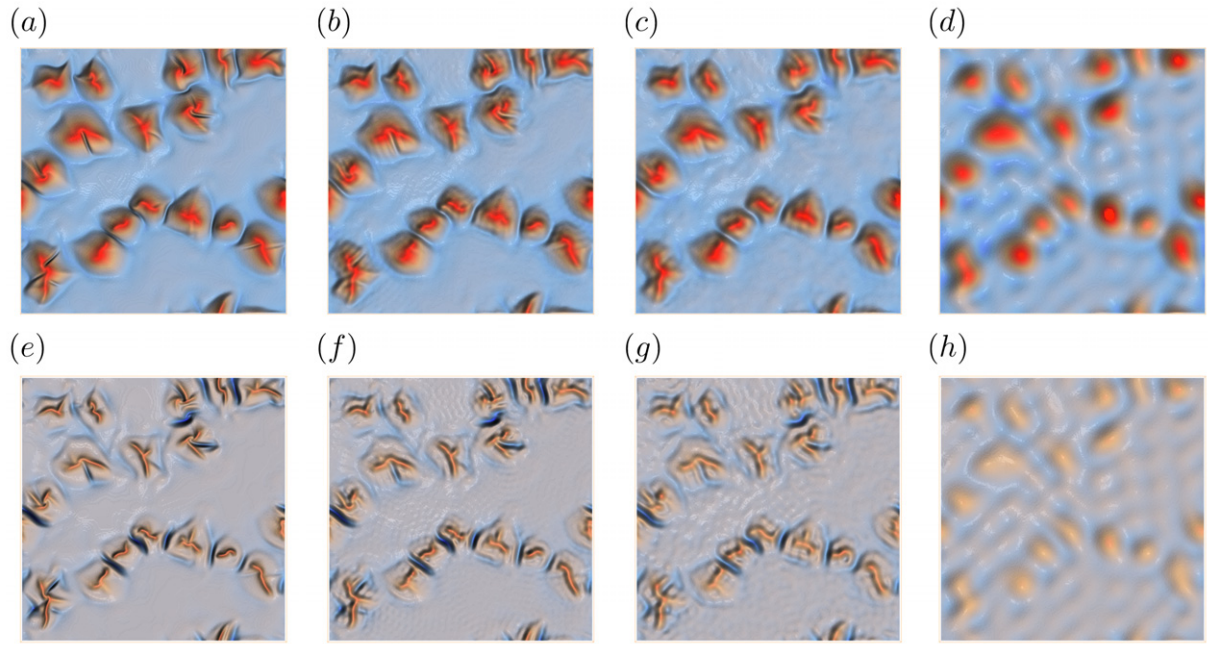

Figure 2. Successive reduction of the degrees of freedom for a snapshot of DNS3. The liquid water content $q_l(\mathbf{x}, t_0)$ at $z = 0.77$ is shown in the upper row. The corresponding vertical velocity $u_z(\mathbf{x}, t_0)$ at $z = 0.5$ in the lower row. Panels (a) and (e) are the original DNS data. Panels (b) and (f) are LDM3a with $N_{\mathrm{DoF}} = 18\,489$ and 99.6% of the total energy. Panels (c) and (g) correspond to $N_{\mathrm{DoF}} = 3021$ containing 95% of the total energy. Finally, panels (d) and (h) correspond to $N_{\mathrm{DoF}} = 159$ which still contain 73.4% of the total energy. For both quantities, the color coding is the same in the four panels: contour levels are between -0.8 and 1 (red) for q_l and between -0.5 and 0.5 (red) for u_z, both in dimensionless units.

3. Successive mode reduction

The DNS runs and the corresponding LDMs with different number of degrees of freedom, N_{DoF}, or modes are listed in table 1. We increase the moist Rayleigh number Ra_{M} by approximately an order of magnitude at fixed aspect ratio $\Gamma = 16$ in runs DNS2, DNS4 and DNS5. Furthermore, we enlarge the convection layer horizontally by factors of two and four in both horizontal directions at fixed Rayleigh number $Ra_{\mathrm{M}} = 1.5 \times 10^4$ in runs DNS1, DNS2 and DNS3. The grid resolutions (N_x, N_y, N_z) have been chosen as follows: for DNS1 we took (64, 64, 17), for DNS2 (128, 128, 17). The grid size for DNS3 was set to (256, 256, 17) while DNS4 and DNS5 were run on a grid with (256, 256, 33) points. As already said, the Rayleigh numbers remain rather small in the present study since a main emphasis is to obtain large aspect ratios $\Gamma \geqslant 8$ as necessary for the cloud formation in the conditionally unstable regime (see e.g. [18]).

A typical set of POD modes in the LDM is shown in figure 3. Since the number of degrees of freedom is eventually finite, the set of horizontal Fourier wave vectors in combination with the quantum numbers for the POD modes form a discrete finite set. Each element of this set can be identified with a vertex on a three-dimensional grid. In the panels of figure 3 each entry to

Table 1. List of performed DNS runs and the corresponding LDMs. In all cases $Ra_D = -Ra_M/3$, $Pr = 0.7$ and $CW_0 = CW_H = 0$. We list the aspect ratio Γ, the moist Rayleigh number Ra_M, the ratios $\Lambda(E)$ and $\Lambda(Nu_M)$ (see equation (18) for both) and the measure Q_1 (see equation (19)) all of which are defined in the text. Averages $\langle E\rangle_t$ and $\langle Nu_M\rangle_t$ (see equation (17)) compare mean energy and buoyancy flux of the original DNS and the corresponding LDMs, respectively. N_{DoF} display the number of degrees of freedom. The additional number for runs LDM3a, LDM4a and LDM5a indicates the number of modes that have been used to evaluate the buoyancy in the physical space in order to accelerate the time advancement. The asterisk in the first column indicates if an additional modal viscosity was used. Note that LDMv1a, LDMh1a and LDM1a are identical and have been tripled for better readability.

	Γ	Ra_M	$\Lambda(E)$	$\Lambda(Nu_M)$	Q_1	$\langle E\rangle_t$	$\langle Nu_M\rangle_t$	N_{DoF}
DNS1	8	1.5×10^4	1	1	0	4.19	1.687	30 547
LDMv1a	8	1.5×10^4	0.994	0.997	0.0042	4.14	1.702	895
LDMv1b	8	1.5×10^4	0.991	0.998	0.0053	4.17	1.699	736
LDMv1c	8	1.5×10^4	0.987	1.000	0.0091	4.10	1.722	577
LDMv1d	8	1.5×10^4	0.975	1.003	0.0189	3.41	1.824	418
LDMv1e	8	1.5×10^4	0.958	1.002	0.0284	5.89	2.236	259
LDMh1a	8	1.5×10^4	0.994	0.997	0.0042	4.14	1.702	895
LDMh1b	8	1.5×10^4	0.993	0.996	0.0057	4.15	1.684	735
LDMh1c*	8	1.5×10^4	0.991	0.995	0.0063	4.16	1.680	595
LDMh1d	8	1.5×10^4	0.988	0.992	0.0082	4.22	1.685	475
LDMh1e	8	1.5×10^4	0.983	0.989	0.0109	4.25	1.692	367
LDMh1f	8	1.5×10^4	0.974	0.983	0.0157	4.60	1.710	271
LDMh1g	8	1.5×10^4	0.953	0.970	0.0267	4.97	1.755	175
LDM1a	8	1.5×10^4	0.994	0.997	0.0042	4.14	1.702	895
LDM1b	8	1.5×10^4	0.977	0.994	0.0154	3.13	1.714	220
LDM1c	8	1.5×10^4	0.977	0.994	0.0154	4.28	1.737	220
LDM1d	8	1.5×10^4	0.869	0.946	0.0700	4.92	1.817	23
DNS2	16	1.5×10^4	1	1	0	12.87	1.543	120 637
LDM2a	16	1.5×10^4	0.996	0.999	0.0029	14.93	1.642	4831
LDM2b	16	1.5×10^4	0.977	0.999	0.0186	12.22	1.476	1238
DNS3	32	1.5×10^4	1	1	0	51.45	1.540	485 320
LDM3a	32	1.5×10^4	0.996	0.997	0.0057	53.12	1.564	18 489 (12 463)
LDM3b	32	1.5×10^4	0.974	0.985	0.0158	53.86	1.761	4937
LDM3c*	32	1.5×10^4	0.974	0.985	0.0158	58.88	1.577	4937
DNS4	16	6.6×10^4	1	1	0	10.68	1.663	970 640
LDM4a	16	6.6×10^4	0.995	0.996	0.0071	10.90	1.669	15 233 (11 997)
LDM4b	16	6.6×10^4	0.978	0.998	0.0186	6.32	1.561	5627
DNS5	16	1.17×10^5	1	1	0	9.485	1.671	970 640
LDM5a	16	1.17×10^5	0.995	0.996	0.0148	10.17	1.711	23 161 (12 749)
LDM5b	16	1.17×10^5	0.979	0.997	0.0186	6.15	1.499	8271

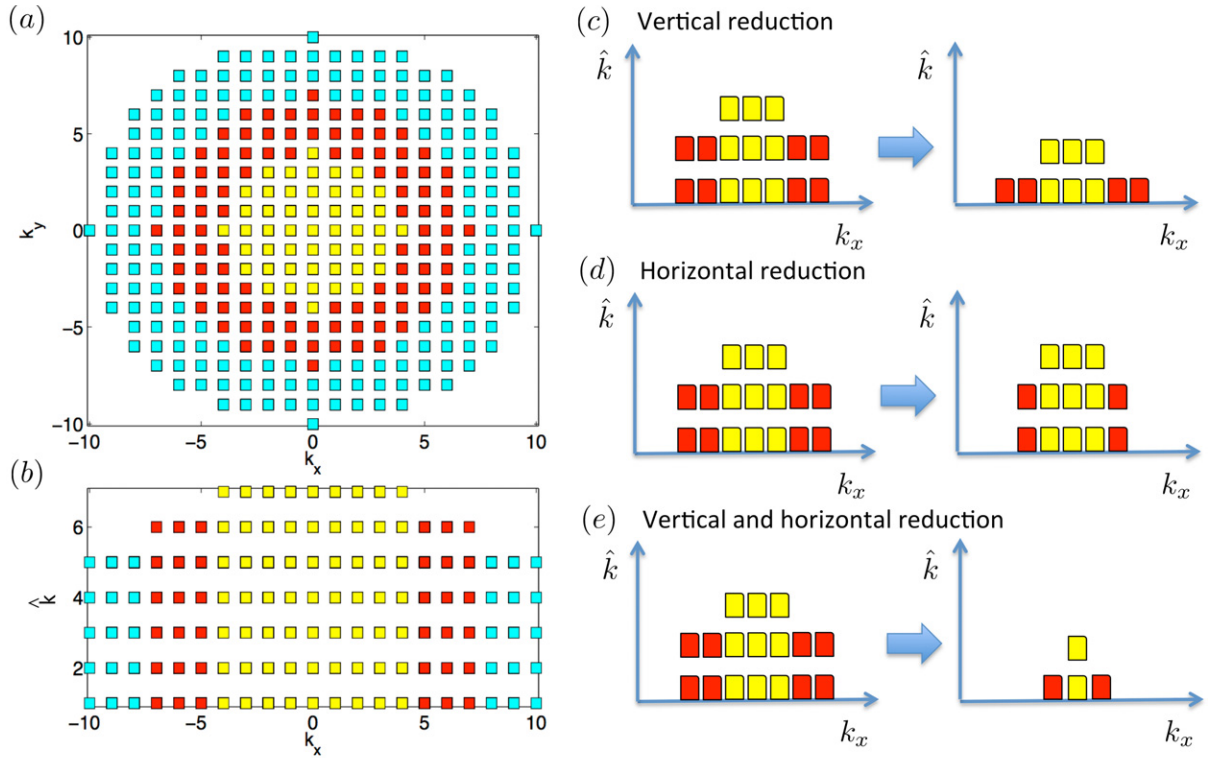

Figure 3. Illustration of the finite set of horizontal Fourier wave numbers and vertical quantum numbers as following for model LDM1a. Each entry $(k_x, k_y, \hat{k})$ is marked by a colored box. (a) Horizontal modes of LDM1a in the $k_x - k_y$ plane are displayed at $\hat{k} = 1$. (b) Modes in the $\hat{k} - k_x$ plane at $k_y = 0$, again for model LDM1a. The different colors highlight different subsets, e.g. entries in yellow show all horizontal wave numbers which are combined with quantum numbers $\hat{k} \leqslant 7$. In panels (c)–(e), we sketch the possible mode reduction strategies which we applied. (c) Sketch of the vertical mode reduction at sustained horizontal resolution. (d) Sketch of the horizontal mode reduction strategy at sustained vertical POD mode resolution. (e) Sketch of the combined vertical and horizontal mode reduction strategy.

this wave vector grid is marked by a little colored box. Panel (a) shows all horizontal Fourier wave vectors which have been used in run LDM1a (see table 1). The three subsets in the figure contain different maximum quantum numbers $\hat{k}$ and have been colored differently therefore. The complementary view to the wave vector set is provided by panel (b) which combines Fourier wave and quantum numbers of the POD modes. The total number of grid entries is 1783 for the present example. Due to the reality condition $a_{\boldsymbol{k}}^{(\hat{k})} = a_{-\boldsymbol{k}}^{(\hat{k})*}$ this results eventually in 895 (=(1783−7)/2+7) degrees of freedom for our example. In all models the entries form concentric cylindrical blocks.

The successive reduction can proceed in three different ways which we want to investigate in the next sections, a vertical reduction that keeps the set of horizontal wave numbers (sketched in panel (c) of figure 3), a horizontal reduction that keeps the set of vertical quantum numbers (sketched in panel (d) of figure 3) and a joint vertical and horizontal reduction as seen in panel (e)

of figure 3. The particular choice of the mode set was motivated by two points. On the one hand, one is interested in the most energetic large-scale modes which represent the major part of the energy. On the other hand, one has to assure an optimal coupling between the modes in the truncated set. The second point requires to include less energetic degrees of freedom which transmit energy between larger-scale modes. Finally one needs a couple of small-scale modes which dissipate the cascading energy. This strategy avoided the use of an additional modal dissipation which was necessary in a few cases only (see section 3.3).

Before we continue with the particular mode set reductions we want to stress once more that the strict ordering of the POD mode set is done with respect to their specific energy. As we outlined already in section 2.2, the three-dimensional POD modes consist of a combination of horizontal Fourier modes and vertical modes. Nevertheless, it holds for all spatial directions that an increase of wave or quantum numbers will pick up structures in the turbulent fields with a smaller energy. Therefore a truncation of modes with a higher wave or quantum number will be generally in line with an increasingly insufficient resolution of smaller-scale turbulent structures.

3.1. Reduction with respect to vertical direction

The LDMs in the next three sections start from DNS1. For the first series of LDMs which is entitled by LDMv, we reduce the modes or degrees of freedom with respect to the vertical direction only. This is done as follows: for horizontal wave numbers $k = |\boldsymbol{k}| = (k_x^2 + k_y^2)^{1/2}$ with a circular shell of radius $k \leqslant k_h$ we take successively less vertical POD modes, e.g. for $k \leqslant 4$ we take $\hat{k} = 7$ in LDMv1a and reduce it to $\hat{k} = 3$ for LDMv1e in steps of one. In a similar way, we proceed for the other shells as sketched in figure 3(c). The starting point of this series, model LDMv1a, has been obtained such that the number of mode couplings is sufficient for resolving advection and dissipation processes. Collecting the most energetic modes only will lead to a model with insufficient energy transfer properties. The couplings are however required to drain the energy down to the smaller scales where dissipation takes over. Therefore, we collect shells in the discrete wave number space which involve enough mode couplings. In the Fourier case, couplings follow from triades $\boldsymbol{k} = \boldsymbol{p} + \boldsymbol{q}$ that can be formed among the wave vectors of the model. A maximization of the number of possible triads causes efficient transfer properties in the model. In this way we might not perform the strongest reduction, but avoid an additional modal dissipation for most of our cases. For the LDMv1a case, global quantities as the total energy E (see equation (11)) or the global mean buoyancy flux, as quantified by the Nusselt number Nu_{M}, come closest to the values obtained from the DNS snapshots. The Nusselt number which adds buoyancy flux by diffusion and convection is defined as

$$Nu_{\mathrm{M}} = 1 + \sqrt{Pr\,Ra_{\mathrm{M}}}\langle u_z M' \rangle_{V,t} \,. \tag{17}$$

The quantities $\Lambda(E)$ and $\Lambda(Nu_{\mathrm{M}})$ yield the fraction that the LDM modes contribute to the corresponding quantity in comparison to the full DNS mode set. Both quantities are evaluated by a successive projection of the POD modes onto a sequence of DNS snapshots and are given by

$$\Lambda(E) = \left\langle \frac{E}{E^{\mathrm{DNS}}} \right\rangle_t, \quad \Lambda(Nu_{\mathrm{M}}) = \left\langle \frac{Nu_{\mathrm{M}}}{Nu_{\mathrm{M}}^{\mathrm{DNS}}} \right\rangle_t . \tag{18}$$

An optimal coupling between the POD modes assures that the energy can be drained from large-scale modes down to small-scale modes efficiently. If this point is not considered, the reduced

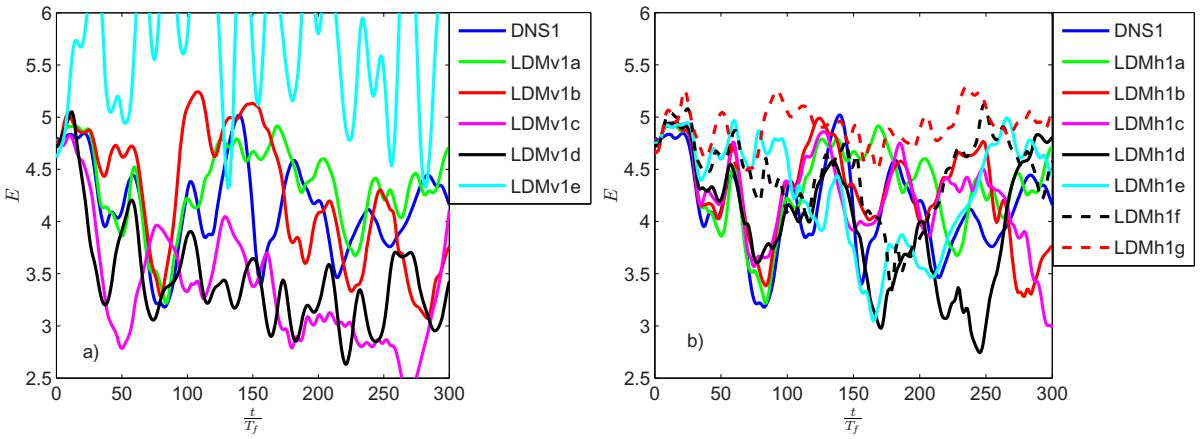

Figure 4. Time evolution of the total energy for the first 300 freefall time units. (a) runs LDMv1a to LDMv1e. (b) runs LDMh1a to LDMh1g which are discussed in section 3.2.

model can be forced into different dynamical regimes or even fixed points as demonstrated by Aubry *et al* [35] for wall-bounded shear flows or by Crommelin and Majda [36] for the Charney–De Vore atmospheric circulation model.

The dynamic evolutions of the different LDM runs result in new time averages for global quantities which we denote by $\langle E\rangle_t$ and $\langle Nu_{\mathrm{M}}\rangle_t$, respectively. They will not perfectly agree with the values which are found for the DNS, but should not deviate too much. These quantities are also listed in table 1. In addition, it is determined how well the buoyancy is resolved. Therefore, the measure Q_1 is defined which quantifies the deviation of the buoyancy as obtained from the set of POD modes (and as used later in the corresponding LDM) to the original DNS data. This measure is given by

$$Q_1 = \left\langle \frac{\| B^{\mathrm{DNS}} - B^{\mathrm{LDM}} \|^2}{\| B^{\mathrm{DNS}} \|^2} \right\rangle_t . \tag{19}$$

All LDM and DNS runs are performed for at least 3000 freefall time units in the statistically stationary regime of the convective turbulence. The freefall time $T_{\mathrm{f}} = \sqrt{(M_0 - M_H)H}$ is the convective time unit in the present problem.

The time evolution of the total energy of the LDM runs is compared in figure 4 for the first 300 freefall times. The runs LDMv1a to LDMv1c oscillate about nearly the same mean values $\langle E\rangle_t$ which are listed in table 1. Note that run LDMv1a, which yields already a mode reduction by a factor of 40, reproduces the energy evolution well. One can see that the deviations of $E(t)$ grow as the reduction is increased. In run LDMv1e the vertical mode reduction has been advanced so far that the energy remains accumulated at the large-scale modes and cannot be drained down to the smaller scales since vertical couplings are missing. This causes larger fluctuations accompanied by a larger mean energy.

Figure 5 compares the height dependence of several quantities. The function $1_{q_{\mathrm{l}}>0}$ is an indicator function, which is one for all points $\mathbf{x}$ inside the clouds, i.e. where $q_{\mathrm{l}} > 0$, and zero otherwise. Horizontal and time averages are combined in order to obtain the graphs in this figure. Inside the cloud the moist warm air rises up. Consequently the mean vertical velocity is larger than zero (panel (a)). This process is accompanied with an upward flux of liquid water,

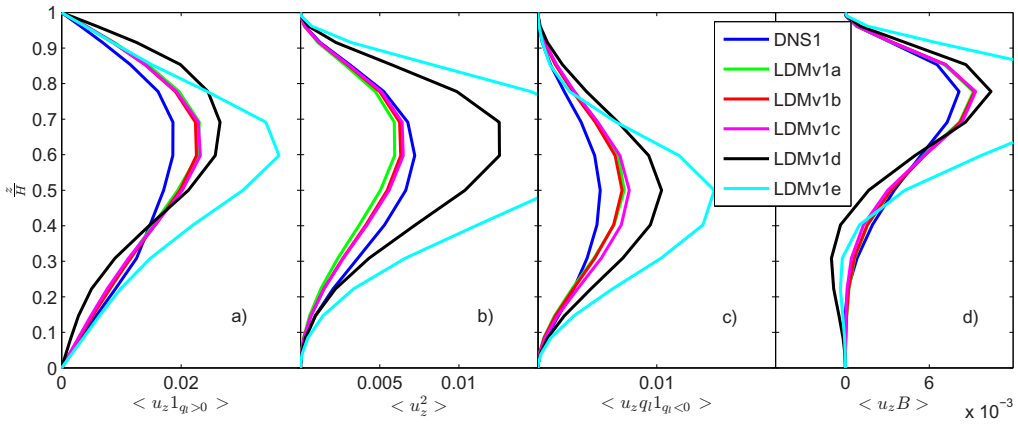

Figure 5. Vertical profiles for mean quantities that characterize the global buoyancy transport across the layer and the clouds which are formed. These are from left to right: (a) vertical velocity inside the clouds, (b) vertical velocity fluctuations across the convection layer, (c) liquid water flux outside the clouds, and (d) convective buoyancy flux across the whole layer. Mean profiles are obtained as combined horizontal and time averages for a time interval of 3000 freefall time units. Vertical mode reduction is applied only.

i.e. it holds mostly $u_z > 0$ and $q_l > 0$. In panel (c), we plot the correlations between vertical velocity and liquid water content outside the clouds, the region of the downdrafts. Since $u_z < 0$ and $q_l < 0$ is obtained there, one ends again with positive amplitudes of the joint correlation $\langle u_z q_l 1_{q_l<0} \rangle$. Physically this correlation means that unsaturated air is pushed downward. Slightly enhanced vertical velocity fluctuations are found in the upper half of the convection layer where the clouds are preferentially formed. Furthermore, we show the vertical velocity fluctuations across the whole layer (panel (b)) and the resulting buoyancy flux (panel (d)).

As discussed at the beginning, the moist convection layer is conditionally unstable. This means that the air is stably stratified outside the clouds which corresponds to a dry buoyancy flux $\langle u_z D' \rangle < 0$. Unstable stratification of the moist air inside the clouds causes a positive buoyancy flux $\langle u_z M' \rangle > 0$. The resulting buoyancy flux $\langle u_z B \rangle > 0$ is shown in figure 6 for DNS3. In panels (b) to (d) of the same figure we display horizontal cuts of the moist convection layer of the same snapshot in order to underline this picture. Local minima of $u_z D'$ and maxima of $u_z M'$ are directly correlated due to the synchronicity relation (8).

The comparison of the five LDM runs confirms the finding of figure 4. While the first three runs LDMv1a to LDMv1c approximate the global transport reasonably well, runs LDMv1d and LDMv1e deviate increasingly. This is also quantified by Q_1 and the Nusselt number $\langle Nu_M \rangle_t$, both of which are given in table 1. All mean profiles display amplitudes which are enhanced with progressing mode reduction. This is a manifestation of an increasing number of missing vertical couplings which are essential for the transport across the layer. Recall that the quantum number for the vertical direction is correlated with the energy of the particular modes. Once they are removed the cascading energy cannot be dissipated efficiently. Energy is accumulated at the large scales.

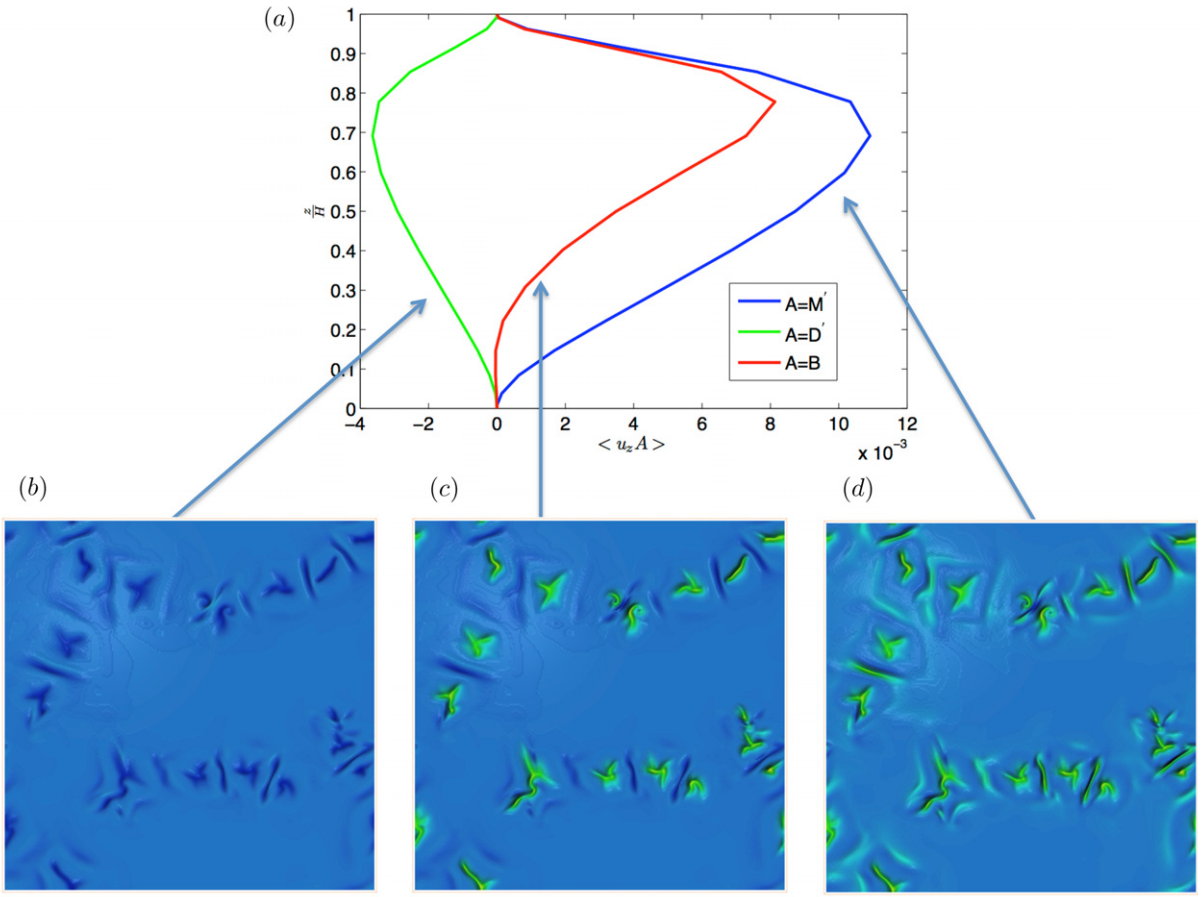

Figure 6. Mean vertical profiles of the dry, moist and total buoyancy fluxes in (a). Data are for DNS3. Contourplot of a snapshot of $u_z D'$ (b), $u_z B$ (c) and $u_z M'$ (d). Data are taken at the same time at $z = 1/2$. The color scale is the same in all three panels. The minimum in deep blue corresponds with -0.078 and the maximum in yellow/green with 0.21. One can clearly see that $u_z D'$ is negative, particularly in the cloud aggregates, exactly where $u_z M'$ is maximized. This results in an upward convective buoyancy flux in the clouds.

3.2. Reduction with respect to horizontal direction

In a next step, we leave the vertical resolution unchanged and reduce degrees of freedom with respect to the horizontal wave numbers. This strategy is sketched in figure 3(d). The total energy for this series of LDM runs which are denoted as LDMh1x is displayed in panel (b) of figure 4. It can be seen that the energy in the different runs remains much closer together, even when the number of degrees of freedom is significantly smaller compared to the series with the vertical mode reduction. This way of reduction seems to be more robust which is also confirmed when the vertical mean profiles of the four quantities are replotted here, similar to those of figure 5. Well resolved vertical couplings among modes seem to be more important for the energy transport than the horizontal mode couplings. The deviations from the original fully resolved data which can be observed in figure 7 remain much smaller. It is, however, clear that

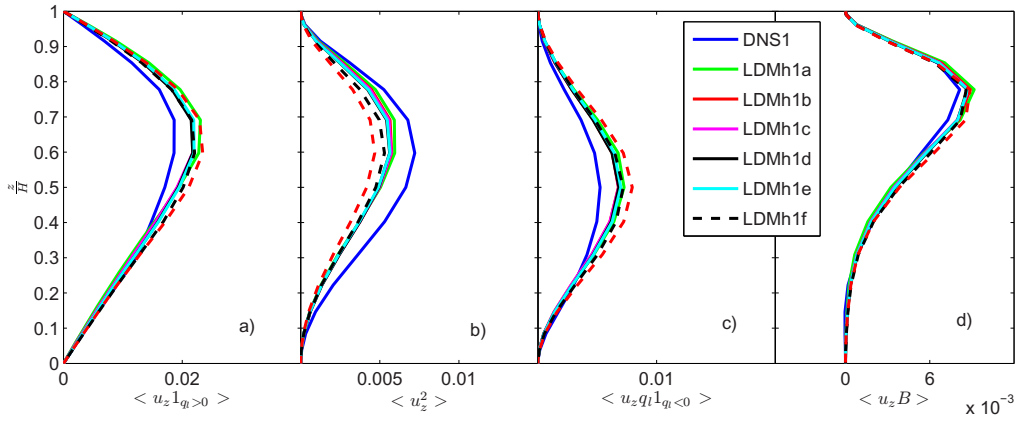

Figure 7. Vertical profiles for mean quantities that characterize the global buoyancy transport across the layer and the clouds which are formed. These are from left to right: (a) vertical velocity inside the clouds, (b) vertical velocity fluctuations across the convection layer, (c) liquid water flux outside the clouds and (d) convective buoyancy flux across the whole layer. Mean profiles are obtained as combined horizontal and time averages for a time interval of 3000 freefall time units. Horizontal mode reduction is applied only.

this way of reduction can also not be continued much further, since the horizontal patterns will be increasingly smeared out such that at some level the volume fraction of clouds and plumes is artificially enhanced which will alter the global transport eventually. The question which we address therefore in the next section is if a further joint reduction of vertical and horizontal degrees of freedom can result in a better LDM.

3.3. Joint vertical and horizontal mode reduction

We start with the same DNS data as in the last sections, but reduce vertical and horizontal modes jointly. The total energy versus time was again compared among the different levels of mode reduction. The findings are similar to the previous two reduction steps. The same holds for the vertical profiles which we show again in figure 8. A further reduction to a number of degrees of freedom below $N_{\mathrm{DoF}} \approx 250$ causes larger deviations from the original DNS evolution as seen in the figure for run LDM1b. The same results for the evolution of the total energy $E(t)$ with time. In figure 9 we compare isosurfaces of the snapshots of the cloud boundaries (which are defined by $q_l = 0$) and the vertical velocity component obtained in the DNS with those obtained from the LDMs of the present series. The straightforward reduction from LDM1a to LDM1b introduces spurious finer-scale structures that reduce the turbulent fluctuations and cause a significant deviation of $\langle E \rangle_t$. We also observe that the cloud field for LDM1b differs significantly. This behavior is also underlined by the enhanced vertical velocity fluctuations which we detected in figure 8. As a consequence, it is found that the cover with clouds is enhanced as well.

Such a larger deviation can be compensated by an additional mode-dependent viscosity, which is introduced to the LDM1c leaving all other parameters and the set of modes unchanged

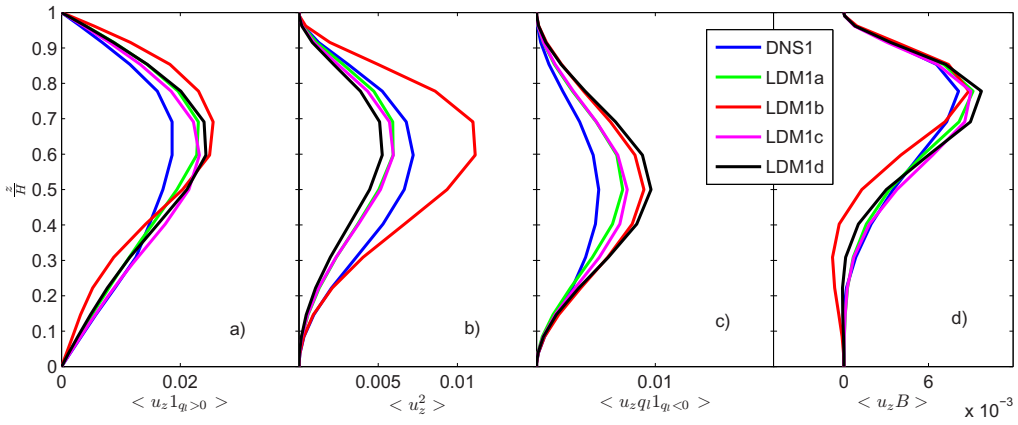

Figure 8. Vertical profiles for mean quantities that characterize the global buoyancy transport across the layer and the clouds which are formed. These are from left to right: (a) vertical velocity inside the clouds, (b) vertical velocity fluctuations across the convection layer, (c) liquid water flux outside the clouds and (d) convective buoyancy flux across the whole layer. Mean profiles are again obtained as combined horizontal and time averages for a time interval of 3000 freefall time units. Horizontal and vertical mode reduction is applied jointly.

in comparison to model LDM1b. Therefore, the equations of motion (16) are modified to

$$\frac{\mathrm{d}a_{\boldsymbol{k}}^{(\hat{k})}}{\mathrm{d}t} = \sum_{\substack{\boldsymbol{p}=\boldsymbol{k}-\boldsymbol{q} \\ \hat{p}=\hat{k}-\hat{q}}} N(\boldsymbol{k},\boldsymbol{q},\hat{k},\hat{q}) a_{\boldsymbol{q}}^{(\hat{q})} a_{\boldsymbol{p}}^{(\hat{p})} + L(\boldsymbol{k},\hat{k}) a_{\boldsymbol{k}}^{(\hat{k})} - \nu(\boldsymbol{k})\boldsymbol{k}^2 a_{\boldsymbol{k}}^{(\hat{k})} + B(\boldsymbol{k},\hat{k}). \tag{20}$$

Additional modal viscosities have been applied successfully in classical Rayleigh–Bénard convection [23] and in cavity flows [37]. The magnitude of the viscosity, which compensates the missing mode couplings and the resulting missing dissipation on small-scales, is chosen such that the LDM simulation is in a statistically stationary regime that corresponds with the one of the original DNS in terms of the mean energy. For each POD expansion coefficient in the LDM, the additional (modal) dissipation is quantified such that $\langle \partial_t a_{\boldsymbol{k},\hat{k}}\, a^*_{\boldsymbol{k},\hat{k}} \rangle_t = 0$ holds again as in the original DNS. For the moist convection system in large-aspect ratio cells it turned out to be more advantageous to use a simpler modal viscosity that depends on the horizontal wave numbers $\boldsymbol{k}$ only and is given by

$$\nu(\boldsymbol{k}) = 1_{|\boldsymbol{k}|-k_c>0}\,[|\boldsymbol{k}| - k_c]\,\alpha, \tag{21}$$

where k_c is a cutoff wave number and α is a control factor. The smaller the scales the more artificial dissipation is present. Run LDM1b was repeated with this additional energy sink ($\alpha = 0.2$ and $k_c = 2$) as run LDM1c. The additional viscosity improves the agreement of the resulting flow structures with those of the DNS, as shown in figure 9. A further reduction to model LDM1d applies a further coarse graining, in particular of the lateral resolution. The draining of the energy proceeds more efficiently since less mode couplings in the smaller set are left unclosed. This allowed us to omit the additional viscosity again. Cloud cover and mean total energy as well as the mean vertical flux profiles are still rather well reproduced in comparison to

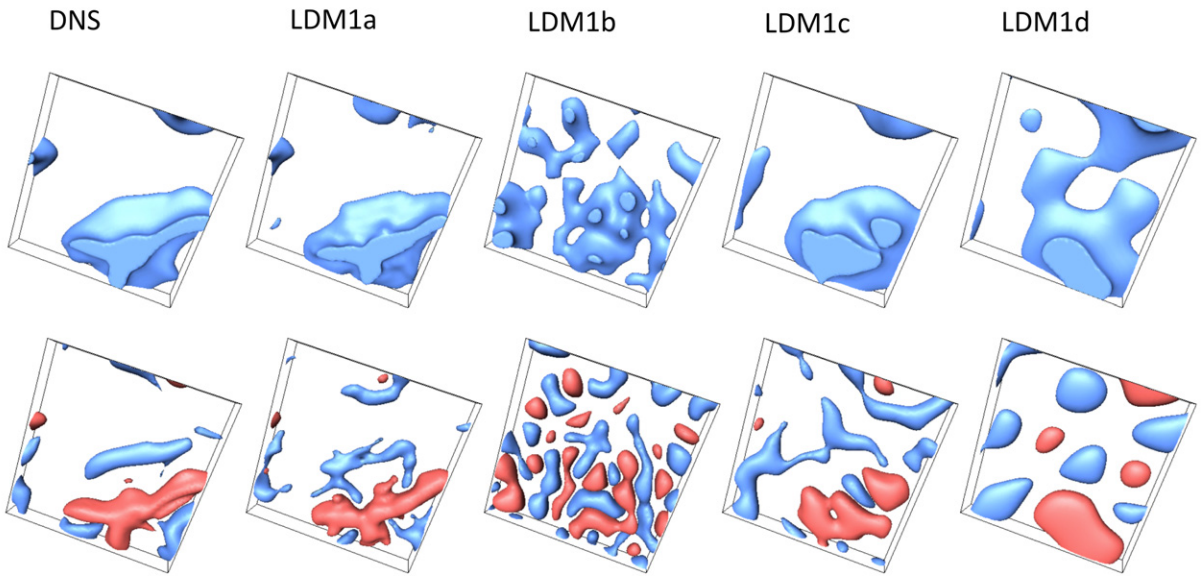

Figure 9. Upper row: isosurfaces of the cloud boundary ($q_l = 0$). Lower row: isosurfaces of the upward (red isosurface, $u_z = 0.05$) and downward vertical velocity component (blue isosurface, $u_z = -0.05$). All plots display a snapshot taken at $t = 50T_f$. The view is from below into the box.

the original DNS run. In figure 10, we summarize the findings up to this point and compare two important global quantities, the mean buoyancy flux $\mathscr{B}$ in panel (a) and the mean cloud cover $\mathscr{C}$ in panel (b) for all three series. Both quantities are defined as

$$\mathscr{B} = \frac{1}{H}\int_0^H \langle u_z B\rangle_{A,t}\,\mathrm{d}z, \tag{22}$$

$$\mathscr{C} = \left\langle \frac{1}{A}\int_A 1_{\overline{q}_l(x,y,t)}\,\mathrm{d}x\,\mathrm{d}y \right\rangle_t, \tag{23}$$

where $1_{\overline{q}_l(x,y,t)}$ indicates if liquid water is present in the column at (x, y, t). The blue solid line in both panels is the reference value from DNS1. This additional comparison underlines clearly our obtained results. A sole successive vertical mode reduction drives the model rather soon away from the DNS results. The horizontal reduction yields more robust regimes that remain closer to the original evolution of the fully resolved DNS. Only a joint reduction, which is partly extended by a modal viscosity can drive the reduction of the degrees of freedom to a limit. The result underlines the importance and necessity of (at least) a coarse approximation of the boundary layers close to the top and bottom. If the remaining vertical degrees of freedom cannot approximate the boundary layer dynamics dynamically, the global transport and thus the cloud cover will increasingly deviate. Although there is no such systematic correspondence between wave number and sampled wavelength as in the Fourier case, a vertical reduction of the mode set has to be advanced more cautiously. This is also caused by the dominant vertical transport inside the clouds for the present convection regime.

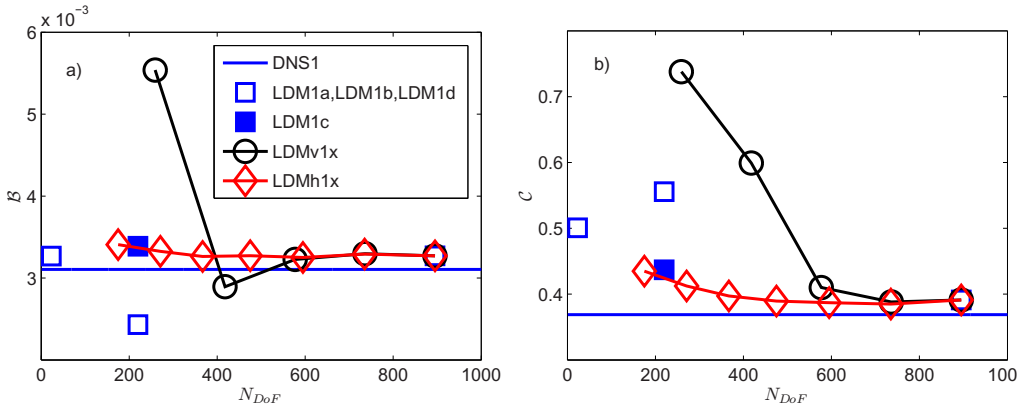

Figure 10. Mean buoyancy flux (a) and mean cloud cover (b) as a function of the mode reduction. All three series are summarized and indicated in the legend. The solid blue line indicates the corresponding DNS value. Recall that LDM1a = LDMh1a = LDMv1a.

3.4. Larger aspect ratios and Rayleigh numbers

In the past sections, we discussed in detail the different strategies of mode reduction and their impact on the global transport properties across the layer for the particular run DNS1 and the resulting LDMs. As visible in table 1 further DNS have been conducted. First, we increased the aspect ratio from $\Gamma = 8$ via 16 up to 32 at fixed Rayleigh number. In this way, we want to see if the approach is capable for extended convection layers which are of interest in view to an application for atmospheric convection. As already stated, our Rayleigh numbers remain rather small. Thus in a second series of DNS, we increased the Rayleigh number at $\Gamma = 16$ up to an order of magnitude. For both ways, mode reduction is done now jointly.

Figures 11(a) and (b) display the mean vertical velocity profiles and the mean convective buoyancy flux as a function of height for DNS at the same Rayleigh number and aspect ratios 8, 16 and 32. The profiles coincide quite well which confirms that an aspect ratio of 8 is sufficiently large to avoid the moist convection being constrained by the finite horizontal extension of the cell. Panels (c) and (d) of the same figure display the Rayleigh number dependence of the same quantities at an aspect ratio of 16. With increasing Rayleigh number the maximum amplitude of both profiles decreases. The same behavior was observed in [14]. With increasing Rayleigh number the mean upward transport inside the clouds decreases. The reason is that the downward diffusion in the stably stratified dry air outside the clouds slows down. Recall that the characteristic time scale, at which the downward transport of the unsaturated air parcels takes place, grows as $t_\mathrm{d} = H^2/\kappa \approx H^2/\nu$. A re-amplification of convective motion in- and outside the clouds can be obtained by the addition of a radiative bulk cooling [34] which breaks the synchronicity between dry and moist buoyancies and was found to destabilize the dry boundary layer outside the cloud aggregates.

The mode reduction and LDM construction in those systems proceeds similarly to what we have discussed in detail for DNS1. Table 1 shows that in all cases the level of mode reduction remains the same, namely about two orders of magnitude at maximum. For some cases, we could accelerate the computations by using a further reduced set of modes to reconstruct the buoyancy field. These mode numbers are bracketed in the table. The trends for the cloud cover

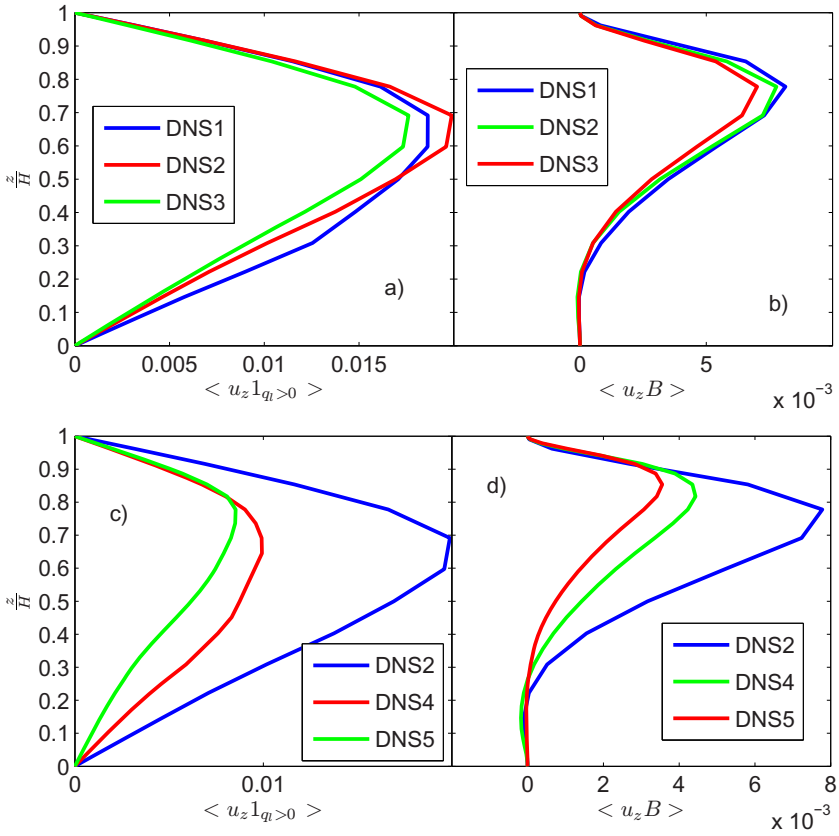

Figure 11. Profiles of the mean vertical velocity inside the clouds (a,c) and of the mean buoyancy flux (b,d) for different DNS runs. The series which consists of DNS1, DNS2 and DNS3 is at a fixed Rayleigh number $Ra_{\mathrm{M}} = 1.5 \times 10^4$ and different aspect ratios. In the second series with DNS2, DNS4 and DNS5 the Rayleigh number is increased at an aspect ratio $\Gamma = 16$ (see also the legend in all panels).

with progressing mode reduction are similar to those that have been shown in figure 10. For example, we observed a slight enhancement for the data at $Ra_{\mathrm{M}} = 6.6 \times 10^4$ and $\Gamma = 16$. While DNS4 yields a value of 26.5%, LDM4a gives 29.7% and LDM4b 33.8% for the cloud cover.

Finally, we display the modal energy spectra of the LDM model in comparison to the fully resolved DNS in figure 12. The spectra are given by

$$\lambda_{\boldsymbol{k}}^{(\hat{k})} = \left\langle \left(a_{\boldsymbol{k}}^{(\hat{k})}, a_{\boldsymbol{k}}^{(\hat{k})} \right)_{L_2} \right\rangle_t . \tag{24}$$

The blue line marks the POD mode spectrum of the fully resolved simulation and the red dots display the spectrum of the corresponding LDM. We show the LDMs for which the reduction has been mostly advanced. All runs are at the same aspect ratio and for increasing Rayleigh number. The POD modes are ordered with respect to their total energy. It can be seen that the LDM spectra fit reasonably well to the DNS data for the first fraction of the spectrum. All LDM spectra decrease less steep for the smaller-scale modes, a manifestation of the accumulation of energy due to missing couplings. Note also that the DNS spectra will continue to decay beyond

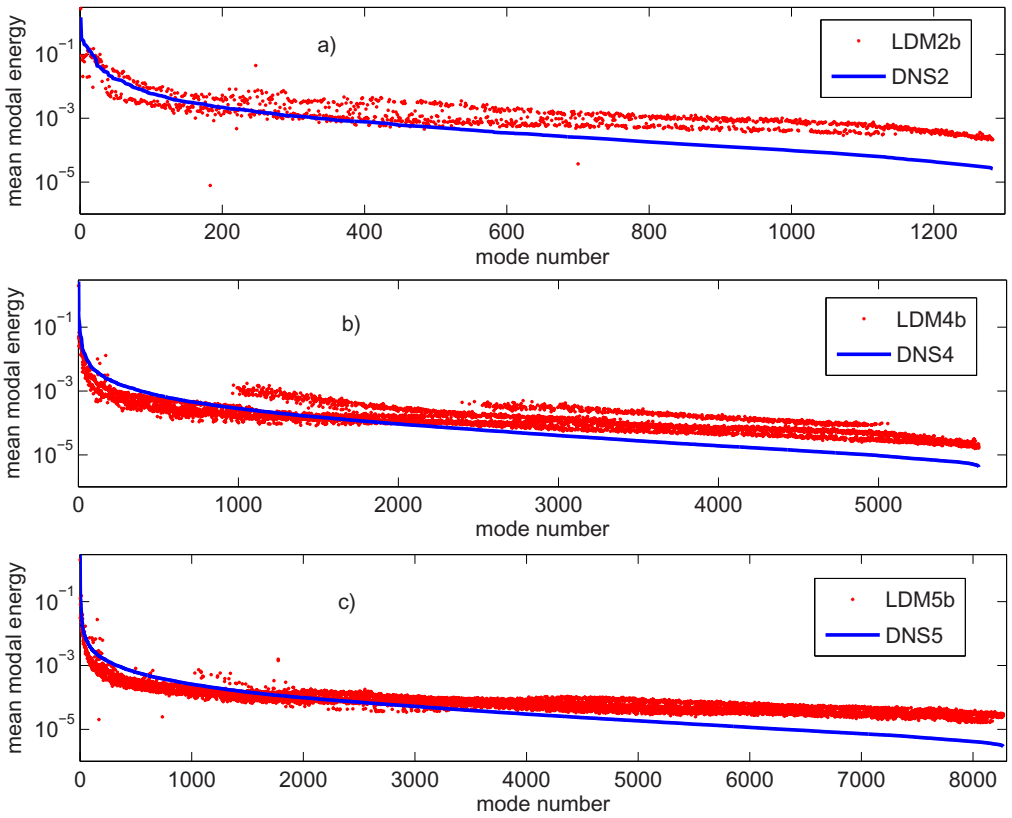

Figure 12. Comparison of the total energy spectra with respect to the POD modes for the full DNS model and the corresponding LDM with the most advanced mode reduction. Data sets are indicated in the legends of the panels. (a) $Ra_{\mathrm{M}} = 1.5 \times 10^4$. (b) $Ra_{\mathrm{M}} = 6.6 \times 10^4$. (c) $Ra_{\mathrm{M}} = 1.2 \times 10^5$. In all cases $\Gamma = 16$.

the range, which is displayed in the panels. The blue lines are plotted here up to the number of degrees of freedom of the LDM only. The three panels indicate also that the decay of the spectra is somewhat slower for larger the Rayleigh number.

4. Summary and outlook

In the present work we studied the impact of the reduction of degrees of freedom (or modes) on the global transport properties for a simple MRBC model in horizontally extended shallow layers. The main ingredient of the model is a linearized thermodynamics at the phase boundary which allows to formulate an explicit saturation condition, given by equation (1). This approach reduces the number of system parameters significantly and defines a cloud formation model with well controlled boundary conditions. The model turns out to be well suited for parametric studies within direct numerical simulations. It is also a well-defined testing bed for the evaluation of different strategies of the reduction of degrees of freedom which have been discussed here. These reduction techniques are applied systematically in the combined wave and quantum number space.

We studied moist convection in the conditionally unstable regime for which the dry and unsaturated air is stably stratified while the moist and saturated air is unstably stratified. Turbulent convection arises when such an equilibrium state is perturbed by a finite amplitude signal. It leads to the formation of localized aggregates of turbulent moist convection which are surrounded by ambient regions in which the turbulence level is significantly reduced. Similar behavior is observed when cumulus clouds are formed by moist convection.

The reduction of degrees of freedom (or of modes) is based on a POD using a sequence of statistically independent snapshots from the original DNSs. The subsequent construction of a LDM which describes the larger-scale dynamics in the convection layer is done by a projection onto the most energetic POD modes and a truncation. Three different strategies of successive truncation have been performed and compared with respect to each other. In detail we performed a vertical mode reduction while keeping the horizontal resolution unchanged and a horizontal mode reduction while keeping the vertical resolution unchanged. Finally, horizontal and vertical degrees of freedom have been reduced jointly. We could show that particularly the vertical reduction has a strong impact on the transport across the layer and the resulting cloud cover. Although the vertical dependencies between quantum number and sampled scales are less straightforward in comparison to the horizontal Fourier modes, POD modes at higher quantum numbers will probe less energetic smaller-scale structures in convective turbulence. Our studies indicate clearly that a sufficient vertical resolution by POD modes is essential. With increasing vertical resolution vertical velocities and thus vertical transport are enhanced (see lower row of figure 2). This agrees with sensitivity investigations in cloud resolving models [28]. The largest possible reduction of the degrees of freedom (by about two orders of magnitude for the parameter sets that were discussed here) is always obtained for a joint horizontal and vertical reduction. For some cases an additional mode-dependent viscosity was applied in the LDM in order to drain the energy which starts to accumulate at the larger scales due to missing mode couplings to the smaller scales.

It is clear that the present geometry and boundary conditions eased the resulting POD mode construction. In particular the translational invariance and the resulting use of Fourier modes simplified the POD framework significantly. This separation caused effectively a vertical POD mode determination only. More realistic simulations of shallow moist convection with heterogenous boundary conditions at the bottom or complex in- and outflows would require a full three-dimensional calculation of the modes and would thus be more demanding. Nevertheless, we believe that the techniques we presented here are applicable to large-eddy simulations since the basic set of equations is qualitatively the same for non-precipitating convection [2].

Our findings complement approaches, such as the so-called super-parameterization in global circulation models [38], which aimed at approximating some aspects of the vertical transport inside a coarse grid cell. We have demonstrated that the LDMs are capable to reproduce significant statistical properties such as the mean buoyancy flux across the layer, the liquid water flux inside the clouds or the cloud cover. Interestingly, we could also detect drastic changes in the cloud structure for intermediate levels of mode reduction. Next possible steps would be to include stochastic terms which mimic truncated fluctuations in these reduced dynamical models or to make a direct comparison with very strongly reduced stochastic transport models [39].

Acknowledgments

This work started while one of us (TW) was still at the TU Ilmenau. The research was supported by the Deutsche Forschungsgemeinschaft under Grant SCHU 1410/8-2 and the Heisenberg program under Grant SCHU 1410/5. We would like to thank Jorge Bailon-Cuba for fruitful discussions at the beginning of this study and Olivier Pauluis for helpful comments.

References

[1] Shaw R A 2003 Particle-turbulence interactions in atmospheric clouds *Annu. Rev. Fluid Mech.* **35** 183–227
[2] Stevens B 2005 Atmospheric moist convection *Annu. Rev. Earth Planet. Sci.* **33** 605–43
[3] Titov D V *et al* 2008 Atmospheric structure and dynamics as the cause of ultraviolet markings in the clouds of Venus *Nature* **456** 620–3
[4] Sánchez-Lavega A *et al* 2008 Depth of a strong jovian jet from a planetary-scale disturbance driven by storms *Nature* **451** 437–40
[5] Sánchez-Lavega A *et al* 2011 Deep winds beneath Saturn's upper clouds from a seasonal long-lived planetary-scale storm *Nature* **475** 71–4
[6] Heintzenberg J and Charlson R J 2009 *Clouds in the Perturbed Climate System* (Cambridge, MA: MIT Press)
[7] Bony S and Dufresne J-L 2005 Marine boundary layer clouds at the heart of tropical cloud feedback uncertainties in climate models *Geophys. Res. Lett.* **32** L20806
[8] Stevens B and Feingold G 2009 Untangling aerosol effects on clouds and precipitation in a buffered system *Nature* **461** 607–13
[9] Satoh M, Matsuno T, Tomita H, Miura H, Nasano T and Iga S 2008 Nonhydrostatic icosahedral atmospheric model (NICAM) for global cloud resolving simulations *J. Comput. Phys.* **227** 3486–514
[10] Moncrieff M W, Waliser D E, Miller M J, Shapiro M A, Asrar G R and Caughey J 2012 Multiscale convective organization and the YOTC virtual global field campaign *Bull. Am. Meteorol. Soc.* **93** 1171–87
[11] Bretherton C S 1987 A theory for nonprecipitating moist convection between two parallel plates. Part I: thermodynamics and 'linear' solutions *J. Atmos. Sci.* **44** 1809–27
[12] Pauluis O and Schumacher J 2010 Idealized moist Rayleigh–Bénard convection with piecewise linear equation of state *Commun. Math. Sci.* **8** 295–319
[13] Mellado J P 2010 The evaporatively driven cloud-top mixing layer *J. Fluid Mech.* **660** 5–36
[14] Pauluis O and Schumacher J 2011 Self-aggregation of clouds in conditionally unstable moist convection *Proc. Natl Acad. Sci. USA* **108** 12623–8
[15] Weidauer T, Pauluis O and Schumacher J 2010 Cloud patterns and mixing properties in shallow moist Rayleigh–Bénard convection *New J. Phys.* **12** 105002
[16] Weidauer T and Schumacher J 2012 Moist turbulent Rayleigh–Bénard convection with Neumann and Dirichlet boundary conditions *Phys. Fluids* **24** 076604
[17] Eckhardt B, Schneider T M, Hof B and Westerweel J 2007 Turbulence transition in pipe flow *Annu. Rev. Fluid Mech.* **39** 447–68
[18] Weidauer T, Pauluis O and Schumacher J 2011 Rayleigh–Bénard convection with phase changes in a Galerkin model *Phys. Rev.* E **84** 046303
[19] Holmes P, Lumley J L and Berkooz G 1996 *Turbulence, Coherent Structures, Dynamical Systems and Symmetry* (Cambridge: Cambridge University Press)
[20] Smith T R, Moehlis J and Holmes P 2005 Low-dimensional modelling of turbulence using the proper orthogonal decomposition: a tutorial *Nonlinear Dyn.* **45** 275–307
[21] Sirovich L and Park H 1990 Turbulent thermal convection in a finite domain: I. Theory *Phys. Fluids* A **2** 1649–58
[22] Sirovich L and Park H 1990 Turbulent thermal convection in a finite domain: II. Numerical results *Phys. Fluids* A **2** 1659–68

[23] Bailon-Cuba J and Schumacher J 2011 Low-dimensional model of turbulent Rayleigh–Bénard convection in a Cartesian cell with square domain *Phys. Fluids* **23** 077101
[24] Giannakis D and Majda A J 2011 Nonlinear Laplacian spectral analysis for time series with intermittency and low-frequency variability *Proc. Natl Acad. Sci. USA* **109** 2222–7
[25] Franzke C, Horenko I, Majda A J and Klein R 2009 Systematic metastable atmospheric regime identification in an AGCM *J. Atmos. Sci.* **66** 1997–2012
[26] Biello J, Khouider B and Majda A J 2010 A stochastic multicloud model for tropical convection *Commun. Math. Sci.* **8** 187–216
[27] Jung J-H and Arakawa A 2004 The resolution dependence of model physics: illustrations from nonhydrostatic model experiments *J. Atmos. Sci.* **61** 88–102
[28] Pauluis O and Garner S 2006 Sensitivity of radiative-convective equilibrium simulations to horizontal resolution *J. Atmos. Sci.* **63** 1910–23
[29] Chillà F and Schumacher J 2012 New perspectives in turbulent Rayleigh–Bénard convection *Eur. J. Phys.* E **35** 58
[30] Siebesma P A *et al* 2003 A large eddy simulation intercomparison study of shallow cumulus convection *J. Atmos. Sci.* **60** 1201–19
[31] Kuo H L 1965 Further studies of the properties of cellular convection in a conditionally unstable atmosphere *Tellus* **17** 413–33
[32] Gryschka M and Raasch S 2005 Roll convection during a cold air outbreak: a large eddy simulation with stationary model domain *Geophys. Res. Lett.* **32** L14805
[33] Moehlis J, Smith T R, Holmes P and Faisst H 2002 Models for turbulent plane Couette flow using the proper orthogonal decomposition *Phys. Fluids* **14** 2493–507
[34] Pauluis O and Schumacher J 2013 Radiation impacts on conditionally unstable moist convection *J. Atmos. Sci.* **70** 1187–203
[35] Aubry N, Holmes P, Lumley J L and Stone E 1988 The dynamics of coherent structures in the wall region of a turbulent boundary layer *J. Fluid Mech.* **192** 115–73
[36] Crommelin D T and Majda A J 2004 Strategies for model reduction: comparing different optimal bases *J. Atmos. Sci.* **61** 2206–17
[37] Cazemier W, Verstappen R W C P and Veldman A E P 1998 Proper orthogonal decomposition and low-dimensional models for driven cavity flows *Phys. Fluids* **10** 1685–99
[38] Grabowski W W and Smolarkiewicz P K 1999 CRCP: a cloud resolving convection parameterization for modeling the tropical convecting atmosphere *Physica* D **133** 171–8
[39] Majda A J and Stechmann S N 2008 Stochastic models for convective momentum transport *Proc. Natl Acad. Sci. USA* **105** 17614–9